INTERNATIONAL JOURNAL OF PRECISION ENGINEERING AND MANUFACTURING Vol. X, No. X, pp. X-XX XXXX 201X / 1
DOI: XXX-XXX-XXXX

Development of a Novel 3-DOF Suspension Mechanism for Multi-function Stylus Profiling Systems

Jia Tian[1], Yanling Tian[1,2,#], Zhiyong Guo[1], Fujun Wang[1], Dawei Zhang[1], Xianping Liu[2], and Bijian Shirinzadeh[3]

1 School of Mechanical Engineering, Tianjin University, Tianjin, 300072, China
2 School of Engineering, University of Warwick, Coventry, CV4 7AL, UK
3 Department of Mechanical and Aerospace Engineering, Monash University, Clayton, VIC3800, Australia
Corresponding Author / E-mail: meytian@tju.edu.cn, TEL: +86-22-27405561, FAX: +86-22-27405561

KEYWORDS : Stylus instrument, Electromagnetic force actuator, Flexure structure, Surface profiling

This paper proposes a novel 3-DOF suspension mechanism for multi-function stylus profiling systems. Incorporating an electromagnetic force actuator, the 3-DOF suspension mechanism provides a controlled loading force. For reasons of the thermal and mechanical stability, a triangular flexure structure is utilized to support the stylus. The stiffness matrix method is used to establish the analytical stiffness model of the 3-DOF suspension mechanism. Considering the 3-DOF suspension mechanism as a 3-DOF lumped-mass-spring system, the dynamic model is established. Finite element analysis (FEA) is used to validate the established static and dynamic models of the 3-DOF suspension mechanism. A prototype is fabricated and experimental tests are carried out to characterize the mechanism's performance. The results show that the 3-DOF suspension mechanism provides a controlled force in a range of up to 10 mN and has a working range in excess of 10 μm with a first natural frequency of 342 Hz in Z axis, indicating good capability for multi-function measurements at the micro/nano scale.

Manuscript received: August XX, 201X / Accepted: August XX, 201X

1. Introduction

It has been widely recognized that surface and subsurface properties at the submicrometre scale will critically influence the design of future generations of components used in engineering, bioengineering and nanotechnology. Most materials exhibit properties in surface regions and at light loads different from those expected of the bulk materials. This property difference can be enhanced to generate a composite material with properties unattainable from the base materials using surface engineering techniques such as plasma nitriding, carburising, etc. Also, the surface topography can be manipulated/patterned to improve the functionality. Applications have been found in industries where component surfaces are patterned to provide a particular function such as Fresnel lenses, anti-reflective structured surfaces and self-cleaning surfaces[1]. In computer disk drives, a landing zone is introduced to eliminate 'stiction' between the flying head and the disk surface, and this parking area is laser machined with many 'bumps' to reduce friction/stiction [2]. The contact mechanism and the effect of surface finish are reasonably understood at a macroscopic level by empirical and statistical methods. However, at the submicrometre level, it is still not clear what is really taking place on the surface during the contact nor how the local surface geometry affects its mechanical and tribological properties.

For the characterization of surface and surface related properties, the available instruments can be categorized into two types, atomic force microscopy (AFM)-based instruments and hardness measurement-based instruments[3]. The AFM-based instruments are capable of providing multi-function measurements at a nanometre/nanonewton level and have already made a great impact on the study of surface topography, tip-sample interaction and mechanical/physical properties[4-9]. However, an AFM has a limited force range because that force is provided by bending its cantilever, which has a typical stiffness of 0.03-3 N/m. Thus, there is no readily available AFM-based microscope offering a loading force up to the mN-scale needed for indentation measurements on most engineered surfaces. The hardness measurement-based instruments can deliver a large range of loading force from newton/millinewton down to micronewton but they are usually utilized to measure hardness/elastic modulus only[10]. Although some nanoindentation instruments have been equipped with a separate AFM/STM to image the surface before and after the indentation, measuring individual functions separately will not give the direct correlated measurements.

The suspension is the most important part of the multi-function stylus profiling instrument, as it affects both the static and dynamic behavior of the measurement system[11-16]. Among the designs of the suspensions, cross-shaped[11, 17] and crab-legged[18-21] flexure structures have been widely utilized to support the stylus. The cross-shaped and crab-legged flexure structures are designed to provide 3-DOF motions: the *Z*-axis translation, *X*- and *Y*- axes rotations. However, the cross-shaped and crab-legged flexure structures are over-constrained structures. The over-constrained boundary conditions cause axial tension; hence the displacement/force relationship can only be linearized at small deflections. In addition, the stress concentration will be more significant. Besides, Gao[22] designed a stylus profiling instrument, where a load-adding cantilever was adopted for surface indentation and a force-sensing cantilever was adopted for profile measurement. However, the dual-cantilever structure was complex and the system suffered from a slower response. In addition, stiffening the cantilever lowered its resolution and also complicated the loading condition as the tip moved in an arc form.

In micro-coordinate metrology applications, the use of triangular flexure structure is now common[23-26]. The triangular flexure structure provides an approximation to 3-DOF motions: the *Z*-axis translation, *X*- and *Y*- axes rotations. In addition to better improvement of thermal and mechanical stability, the rotationally symmetric design intuitively contains a zone of near-constant spring constant, compared to the standard cantilever.

The paper presents a novel 3-DOF suspension mechanism for multi-function stylus profiling systems. The 3-DOF suspension mechanism is expected to provide a working range in excess of 10 μm in *Z* axis with fast response and compact size. A triangular flexure structure is utilized to support the stylus. As a result, the linearity and stability of the mechanism is guaranteed. An electromagnetic force actuator provides a controllable loading force. The stiffness matrix method is used to establish the analytical stiffness model of the 3-DOF suspension mechanism. Considering the 3-DOF suspension mechanism as a 3-DOF lumped-mass-spring system, the dynamic model is established. Finite element analysis (FEA) is used to validate the established static and dynamic models of the 3-DOF suspension mechanism. A prototype is fabricated and experimentally tested to characterize the mechanism's response and performance.

2. Mechanical Design

The schematic diagram of the 3-DOF suspension mechanism is shown in Fig. 1. The general dimension for the mechanism is 36 mm in diameter and 20 mm in total height. The mechanism's components are easy to fabricate and easy to assemble utilizing set screws. The fixing holes in the upper section of the coil former are to hold the mechanism to the instrument within which it is being used. The mechanism can provide 3-DOF motions: the translation in *Z* axis (denoted as *z*), and rotations about *X* and *Y* axes (denoted as θ_x and θ_y, respectively).

Incorporating an electromagnetic force actuator, the mechanism provides a controlled loading force. The electromagnetic force actuator consists of a permanent magnet and a uniformly wound circular cylindrical coil assembly. The magnet is positioned inside the coil with the axis of its magnetic field co-linear with the coil axis. Upon the excitation of the coil, the interaction of the magnetic field gradient of the coil and the permanent magnet produces a force on the latter. A saturated permanent magnet of Neodymium-baron-iron (NdBFe) is used. The 34 guage copper wire is used for the winding of the coil.

The triangular flexure structure contains a central platform and three identical leaf-type flexure hinges. The central platform has three identical arms, which are arranged in a circular pattern with 120° offsets. The three identical leaf-type flexure hinges tangentially touch the arms. The magnet is attached at the center of the central platform. A silica tube is attached on the other side of the central platform, acting as a stylus. The diameter of the silica tube is 2 mm with a thickness of 0.5 mm. In addition to better reduction of stress concentration, the rotationally symmetric design helps to obtain a higher sensitivity and a near-constant spring constant. Thus linearity and stability of the 3-DOF suspension mechanism is guaranteed. The triangular flexure structure is monolithically made of a copper/beryllium (Cu/Be) foil with a thickness of 150 μm. The triangular flexure structure is clamped between two face-ground base plates with an outside diameter of 26 mm and inside diameter of 16 mm. This has the advantage that no heat is introduced during the assembly. Moreover, the contacting area between outer frame of the triangular flexure structure and base plates is flat, so the triangular flexure structure are not bent or distorted by their clamping.

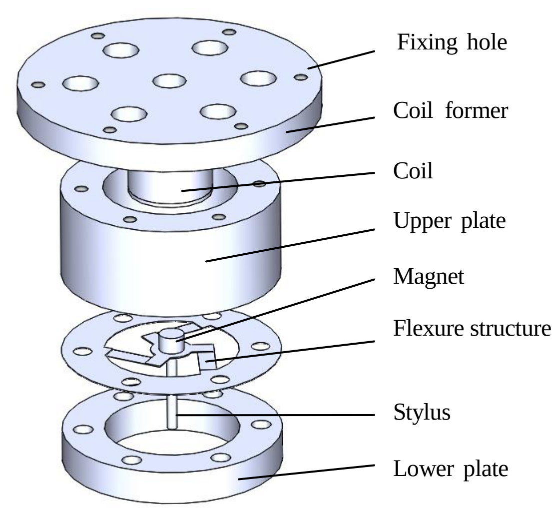

Fig. 1 The schematic diagram of the 3-DOF suspension mechanism

3. Finite Element Analysis of the Electromagnetic Force Actuator

The parameters of the electromagnetic force actuator are defined in Fig. 2. The coil assembly follows the typical rule that the outer

DOI: XXX-XXX-XXXX

diameter of the coil is about equal to its length and twice the inner diameter. It is assumed that radial produced by slight misalignment and the mechanism being driven is much stiffer in torsion than translation. Therefore, based on the electromagnetic theory, the *Z*-axis component of the force *F* experienced by a magnet with a magnetic moment *M* within a field of strength H_z is given by[27-29]

$$F_z = M\frac{dH_z}{dz} \tag{1}$$

where $M = B_{rem}V$ is the magnetic moment of the magnet, B_{rem} is the remanence of the magnet and *V* is the volume of the magnet.

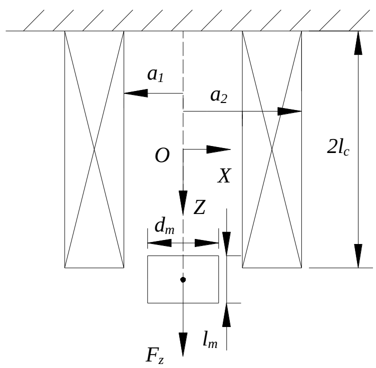

Fig. 2 Parameters of the electromagnetic force actuator

FEA is conducted to investigate the characteristics of the electromagnetic force actuator. ANSYS MAXWELL is chosen to simulate the field strength and the magnetic field gradient of the coil and the produced force on the magnet. Considering that electromagnetic force actuator is axisymmetric along the axis of the coil, a 2-D axisymmetric simulation is performed. The parameters used in the simulation are listed in Table 1.

Table 1 Parameters in the simulation

Parameter	Value
Remanence of this magnet B_{rem} (T)	1.18
Length of the coil $2l_c$ (mm)	10
Inside radius of the coil a_1 (mm)	2.5
Outside radius of the coil a_2 (mm)	5
Turn of the coil N (mm)	400
Length of the magnet l_m (mm)	3
Diameter of the magnet d_m (mm)	2

Fig. 3 (a) and (b) show plots of the magnetic field strength and magnetic field gradient with respect to the position along the axis of the coil. As Fig. 3 (a) shows, the maximum axial field strength H_z occurs at the centroid of the coil. As Fig. 3 (b) shows, the maximum axial field gradient dH_z/d_z occurs at a point just beyond the end of the coil. Fig. 3 (b) gives a basic guide to choose the work position of the magnet, thus we can control the motion of the magnet by controlling the coil current effectively.

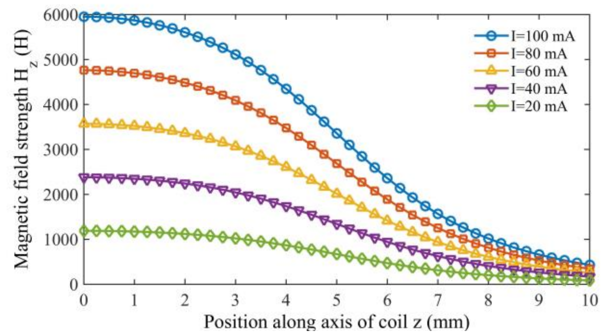

(a) Magnetic field strength

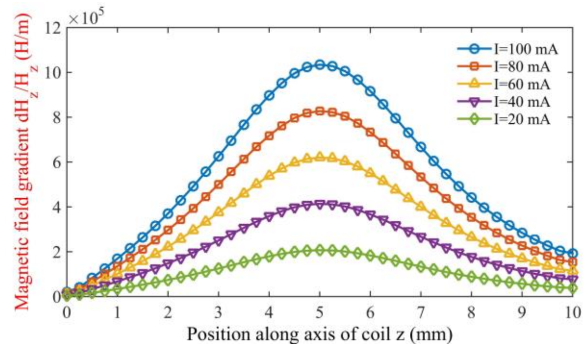

(b) Magnetic field gradient

Fig. 3 Magnetic field strength and gradient along the axis of the coil

FEA is conducted to further investigate the force on the magnet positioned at a point on the axis a distance *z* from the centroid of the coil. As shown in Fig. 4, for small displacements of the magnet, the force experienced by the magnet within the energized coil is proportional to the applied current *I*, which can be expressed as follows：

$$F_z = kI \tag{2}$$

where the constant *k* is a function of the position of the magnet along the axis of the coil. It is noted that *k* obtains a maximum value of 0.14 N/A when the magnet is positioned at *z*=5 mm.

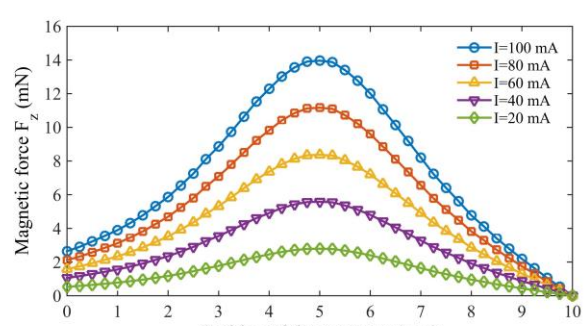

Fig. 4 The force on the magnet at different positions

4. Analytical Stiffness Model of the Mechanism

The triangular flexure structure of mechanism is illustrated in Fig. 5. The three arms of the central platform are identical with a length of

l_a, a width w_a and a thickness of t_a (perpendicular to the *XY* plane, not shown in Fig. 5). The local coordinate for a leaf-type flexure hinge is shown in Fig. 6, where the *z* axis is the symmetry axis of triangular flexure structure and the *y* axis is parallel to its length direction.

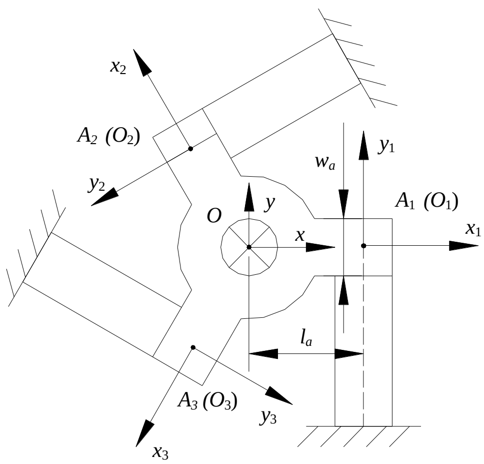

Fig. 5 The triangular flexure structure

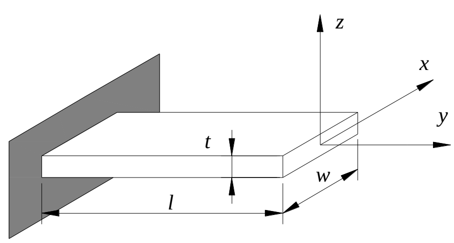

Fig. 6 Local coordinate for a leaf-type flexure hinge

As shown in Fig. 5, the center point of the central platform is labeled as *O*, the arm ends of the central platform are labeled as A_i, (*i* = 1, 2, 3). The load vector at point *O* is defined as

$$D=\begin{bmatrix} F_z & M_x & M_y \end{bmatrix}^T \tag{3}$$

and the displacement vector at point *O* is defined as

$$P=\begin{bmatrix} z & \theta_x & \theta_y \end{bmatrix}^T \tag{4}$$

During the static stiffness modeling of the 3-DOF suspension mechanism, a global coordinate O_0-$x_0y_0z_0$ is located at the initial position of the point *O*; three coordinates O_i-$x_iy_iz_i$, (*i*=1, 2, 3), are located at the initial positions of the points A_i.

For the 3-DOF suspension mechanism, the rotational transformation matrix R_i from the global coordinate O_0-$x_0y_0z_0$ to the coordinates O_i-$x_iy_iz_i$, (*i*=1, 2, 3), is given by

$$R_i=\begin{bmatrix} 1 & 0 & 0 \\ 0 & \cos(\alpha_i) & -\sin(\alpha_i) \\ 0 & \sin(\alpha_i) & \cos(\alpha_i) \end{bmatrix},\quad i=1,2,3 \tag{5}$$

where α_i is the rotation angle from the coordinate O_i-$x_iy_iz_i$ to the global coordinate O_0-$x_0y_0z_0$. Under current configuration, $\alpha_1 = 0$, $\alpha_2 = 2\pi/3$, and $\alpha_3 = 4\pi/3$.

For the 3-DOF suspension mechanism, the translational transformation matrix T_i from the global coordinate O_0-$x_0y_0z_0$ to the coordinates O_i-$x_iy_iz_i$, (i=1, 2, 3), is given by

$$T_i=\begin{bmatrix} 1 & 0 & 0 \\ -y_i & 1 & 0 \\ x_i & 0 & 1 \end{bmatrix},\quad i=1,2,3 \tag{6}$$

where $x_i=l_a\cos(\alpha_i)$, $y_i=l_a\sin(\alpha_i)$.

The stiffness matrix for a leaf-type flexure hinge in its local coordinate is given by[26]

$$k_l=\begin{bmatrix} c_{zz} & ck_{zx} & 0 \\ ck_{zx} & k_{xx} & 0 \\ 0 & 0 & k_{yy} \end{bmatrix} \tag{7}$$

where $c_{zz}=\dfrac{Et^3w}{l^3}$, $ck_{zx}=\dfrac{1}{2}\dfrac{Et^3w}{l^2}$, $k_{xx}=\dfrac{1}{3}\dfrac{Et^3w}{l}$, $k_{yy}=\dfrac{1}{6}\dfrac{Et^3w}{(1+\nu)l}$, *E* is the Young's modulus, and *ν* is the poisson's ratio.

Utilizing stiffness matrix method[30-32], we can obtain the stiffness matrix of the 3-DOF suspension mechanism, which reflects the relationship between the load *D* and displacement *P* both defined at the center point of the central platform, point *O*, as follows:

$$K=\sum_{i=1}^{3}T_i^TR_i^Tk_lR_iT_i \tag{8}$$

Substituting Eqs. (5) – (7) into Eq. (8), the stiffness matrix of the mechanism can be calculated as follows:

$$K=\begin{bmatrix} K_z & 0 & 0 \\ 0 & K_{\theta_x} & 0 \\ 0 & 0 & K_{\theta_y} \end{bmatrix} \tag{9}$$

where

$$K_z=3c_{zz}=\frac{3Et^3w}{l^3} \tag{10}$$

$$\begin{aligned} K_{\theta_x}=K_{\theta_y}&=\frac{3}{2}\left(c_{zz}l_a^2+k_{xx}+k_{yy}\right) \\ &=\frac{3}{2}\frac{Et^3w}{l}\left(\frac{l_a^2}{l^2}+\frac{1}{3}+\frac{1}{6(1+\nu)}\right) \end{aligned} \tag{11}$$

It is noted that the stiffness matrix *K* of the 3-DOF suspension mechanism is diagonal, containing the effective stiffnesses for each degree of freedom.

5. Dynamic Modeling of the Mechanism

In the dynamic modeling of the 3-DOF suspension mechanism, the mass moving with the central platform is denoted as *m*; the moments of inertias about *X* and *Y* axes are denoted as I_x and I_y, respectively; the damping coefficient along *Z* axis is denoted as c_z, and the damping coefficients about *X* and *Y* axes are denoted as c_x and

DOI: XXX-XXX-XXXX

c_y, respectively. Considering the mechanism as a 3-DOF lumped-mass-spring system, based on Newton's second law of motion, the equations of motions of the mechanism can be derived as follows:

$$M\ddot{P} + C\dot{P} + KP = D \tag{12}$$

where $M = diag\ (m, I_x, I_y)$, $C = diag\ (c_z, c_x, c_y)$, D is the load vector at the center point of the central platform as defined in Eq. (3), P is the displacement vector at the center point of the central platform as defined in Eq. (4), K is the stiffness matrix of the mechanism as defined in Eq. (9).

Due to symmetry, the moment of inertia about X axis I_x is equal to the moment of inertia about any other axis in the XY plane. Based on the eigenvalues K_i (i = 1, 2, 3) of the stiffness matrix K, the natural frequencies of the mechanism can be derived as follows:

$$f_i = \begin{cases} \dfrac{1}{2\pi}\sqrt{\dfrac{K_i}{m}} & \text{i=1} \\ \dfrac{1}{2\pi}\sqrt{\dfrac{K_i}{I_x}} & \text{i=2, 3} \end{cases} \tag{13}$$

where f_i (i = 1, 2, 3) are the first three order natural frequencies of the mechanism.

6. Finite Element Analysis of the Mechanism

During the analytical modeling process, the parasitic translations in the length directions of the leaf-type flexure hinges when they are translated out of the XY plane are ignored. Consequently, the actual behavior of the 3-DOF suspension mechanism will be affected. Hence, computational analyses are necessary to evaluate the characteristics of the mechanism and to validate the analytical models established in Sections 4 and 5. Thus FEA is conducted to investigate the static and dynamic characteristics of the developed mechanism and check the modeling errors. ANSYS Workbench is chosen to perform all the modeling and analysis operations.

The cases of the coil assembly, the clamping plates and the six fixing holes are ignored herein to simplify the FEA model. The simplified FEA model is shown in Fig. 7. The simplified model is comprised of three materials: copper/beryllium (Cu/Be), Neodymium-baron-iron (NdBFe), and silica, whose properties are listed in Table 2. The parameters of the triangular flexure structure are listed in Table 3.

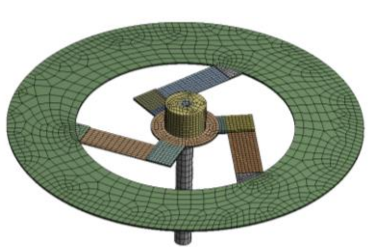

Fig. 7 FEA model of the mechanism

Table 2 Properties of the materials involved in the FEA

	Cu/Be	NdBFe	Silica
Young's modulus E (GPa)	128	160	340
Density ρ (kg/m3)	8300	7500	3600
Poisson's ratio v	0.34	0.24	0.22

Table 3 Parameters of the triangular flexure structure

Parameter	Value
Arm length l_a (mm)	4
Arm width w_a (mm)	2
Arm thickness t_a (μm)	150
Flexure length l (mm)	5.2
Flexure width w (mm)	2
Flexure thickness t (μm)	50

6.1 Static Performance

Fig. 8 (a) shows the mechanism's deformation under a compression load of 10 mN in Z axis. FEA results show the maximum deflection of the mechanism is 15.26 μm and occurs in the central platform; the linear stiffness of the mechanism in Z axis is calculated to be 655.4 N/μm. The maximum elastic deformation of the central platform is 50 nm; this implies the central platform can be treated as rigid component. Fig. 8 (b) further plots the stress distribution of the mechanism. It is found that under a compression load of 10 mN in Z axis the maximum equivalent stress is 10.8 MPa, which is far below the yield strength of the material (over 430 MPa).

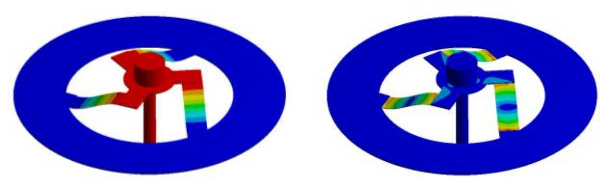

(a) The mechanism's deformation (b) The mechanism's stress distribution

Fig. 8 The mechanism's deformation and stress distribution under a compression load of 10 mN in Z axis

6.2 Dynamic Performance

Block Lanczos method is selected to extract the first 10 modes of the mechanism. The first 3 resonant frequencies and corresponding mode shapes are listed Fig. 9. Theoretically, the resonant frequencies of the mechanism corresponding to the 2st and 3rd mode shapes should be identical. However, due to the inevitable small amount of asymmetry in meshing and the calculation errors in iterations within the software itself, these frequencies show slight difference. The first resonant frequency from FEA is slightly lower than the resonant frequency of 310.9 Hz obtained in the analytical model. This makes sense as analytical model ignores the masses of all the flexure hinges, which results in an underestimation of the total mass and overestimation of the resonant frequency. The mode shapes below 10 kHz have also been investigated. As higher mode shapes are almost impossible to excite, these mode shapes will not be further discussed.

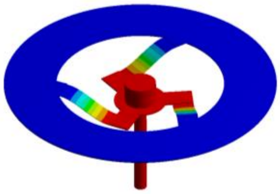

(a) 1st mode: linear motion along axis Z at 304.92 Hz

(b) 2nd mode: rotation about axis X at 471.6 Hz

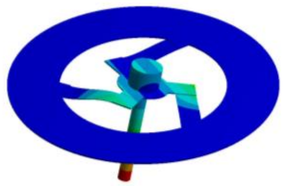

(c) 3rd mode: rotation about axis Y at 471.9 Hz

Fig. 9 Resonant frequencies and mode shapes of the mechanism

7. Experimental Validation

The schematic diagram of the system setup is provided in Fig. 10. The mechanism is attached to a three-dimension manual positioning stage, where three micrometers are used to move the mechanism in X, Y and Z axes, respectively. A specially designed current drive has been built that can provide a highly stable and low noise current for controlling the loading force of the mechanism. The drive current can be varied up to 100 mA with a resolution of 1 mA. A dSPACE DS1103 R&D control board is utilized to provide a real-time control at a sampling rate of 5 kHz. DS1103 communicates with the computer through a PCI bus. The overall system sits on a Newport optical table for the reduction of external disturbances during the experiment process.

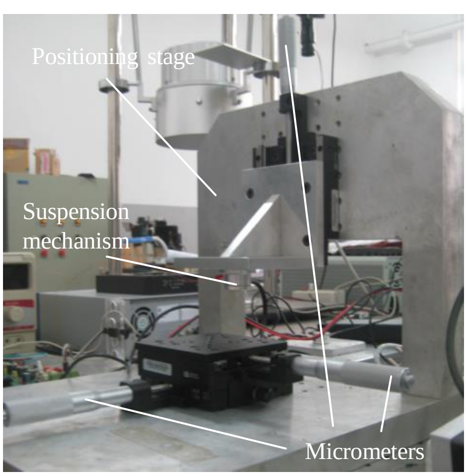

Fig. 10 System setup

7.1 Force calibration and static test

The photograph of the experimental setup for force calibration is provided in Fig. 11 (a). The load cell (F329, Novatech Measurements Limited) has a range of 100 mN with a resolution of 10 μN. The load cell has a mechanical stiffness of 1300 N/m.

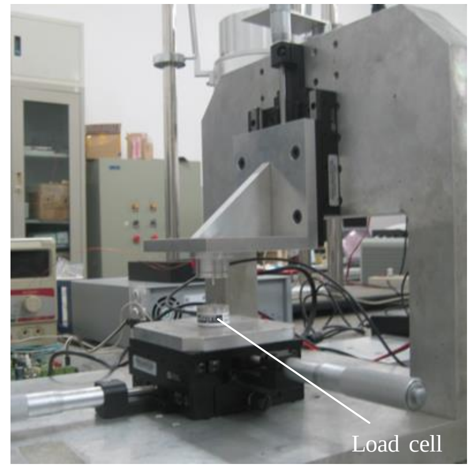

(a) force calibration

(b) static and dynamic tests

Fig. 11 Experimental setup

In the force calibration, the stylus was lowered onto the button of the load cell and adjusted in height until the load cell has an initial output; then a ramp current is sent to the coil to produce an uplift force. The test result of the load cell output against the drive current is plotted in Fig. 12. It is noted that a current of about 80 mA is need to produce a lift force of 6.08 mN.

The relationship between the load cell output F_O and the actual electromagnetic force F_z is given by

$$F_o = F_z \frac{K_L}{K_L + K_z} \tag{14}$$

where K_L = 1300 N/m is the mechanical stiffness of the load cell, K_z is the linear stiffness of the mechanism in Z axis.

Fig. 11 (b) shows the experimental setup for the static test, where the displacement of the central platform is measured by a laser displacement sensor (LK-H050, KEYENCE CORPORATION). In the static test, a set of constant current is sent to the coil. The measured displacement-current curve is provided in Fig. 13.

Based on the experimental results in Fig. 12 and Fig. 13, we can drive the relationship between the electromagnetic force and the displacement of the central platform, which is shown in Fig. 14.

DOI: XXX-XXX-XXXX

Linear curve fitting technique is utilized to derive the linear stiffness of the central platform, which is listed in Table 4. Due to the etching accuracy, the thickness of the leaf-type flexure hinges can not be made accurate enough. Furthermore, the etching process may change the surface quality of the leaf-type flexure hinges in some degree. As a result, there is 28.6% difference between analytical and experimental results.

The sensitivity of the force actuator is derived to be 0.127 N/A. The FEA result is 0.14 N/A in Section 3. The discrepancy between the experimental and the FEA results is strongly dependent on the quality of the coil windings. Even with coils wound by hand, force characteristics to within 10% of the FEA result could be obtained.

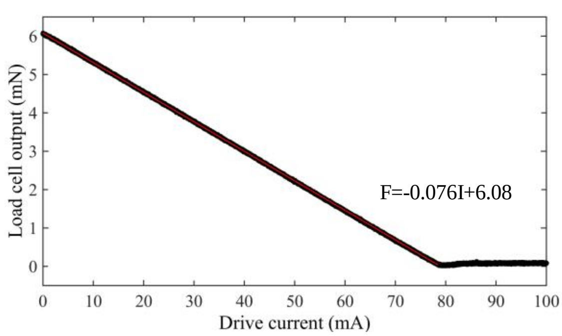

Fig. 12 Load cell output/ current relationship of the central platform

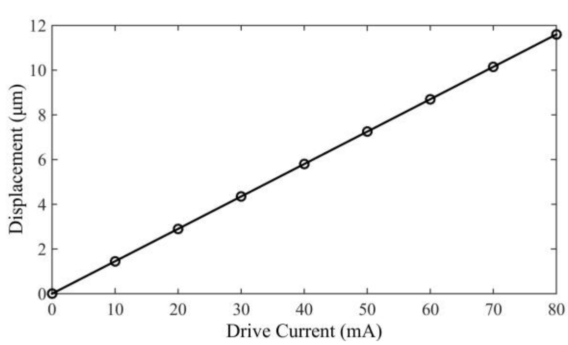

Fig. 13 Displacement/current relationship of the central platform

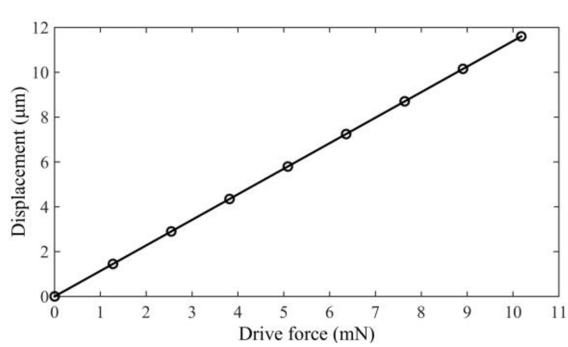

Fig. 14 Displacement/force relationship of the central platform

Table 4 Stiffness of the mechanism in Z axis

Stiffness	Analytical	FEA	Experimental
K_z (N/m)	682.7	655.4	877.8

7.2 Dynamic performance of the mechanism

In order to investigate the dynamic characteristics of the mechanism and validate the analytical models established aforementioned in section 5, experiments are performed to obtain the dynamic performance of the mechanism. Fig. 11 (b) shows the experimental setup for dynamic performance. Excitation of the mechanism with a swept frequency sine wave provides an ideal means to capture information about the mechanism. In the experiment, A sine swept signal in frequency linearly from 1Hz to 1 kHz with an amplitude of 0.025V is generated at DS1103 board as the control voltage; the displacement of the central platform is measured by the laser displacement sensor. Fig. 15 shows the spectra of the measured central platform's displacement. The first natural frequency of the mechanism in Z axis is measured to be 342 Hz and is listed in Table 5, together with the analytical and FEA results as comparison. The gap between the analytical and experimental results is 10%. The gap is smaller than that derived from K_z gap as mentioned in Section 7.1. This makes sense as the dynamic model ignores the masses of all the leaf-type flexure hinges, which results in an underestimation of the total mass and overestimation of the resonant frequency. Another contributing factor for this could be that the clamping of the triangular flexure structure by the two face-ground base plates is not tight enough.

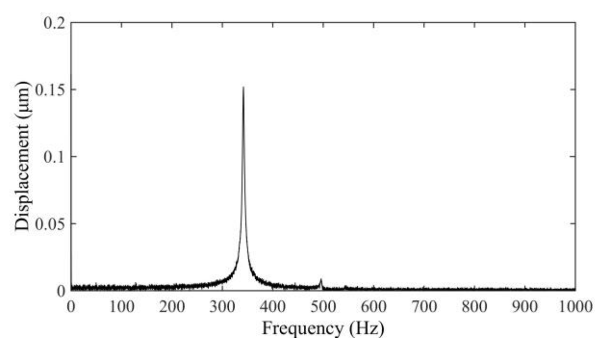

Fig. 15 Spectra of the measured central platform's displacement

Table 5 First natural frequency of the mechanism

First natural frequency	Analytical	FEA	Experimental
f_1 (Hz)	310.9	304.9	342

7.3 Tracking Trajectories

Experiments have been conducted to track two triangular trajectories with frequencies of 0.5 Hz and 5 Hz. The tracking results are shown in Fig. 16 and Fig. 17. In the case of tracking 0.5 Hz triangular trajectory, the maximum tracking error is 0.695 μm (about 5.99% of the total traveling range of the desired trajectory). In the case of tracking 5 Hz triangular trajectory, the maximum tracking error is 0.907 μm (about 7.82% of total traveling range). Due to the hysteresis effect of the electromagnetically-driven mechanism, the actual displacement of the central platform can not return to the origin. It is noted that when the frequency increases, the tracking performance decreases a little. In both cases, the maximum tracking errors occur at the turning points of the reference trajectory, where the modal vibration of the mechanism is likely to be excited.

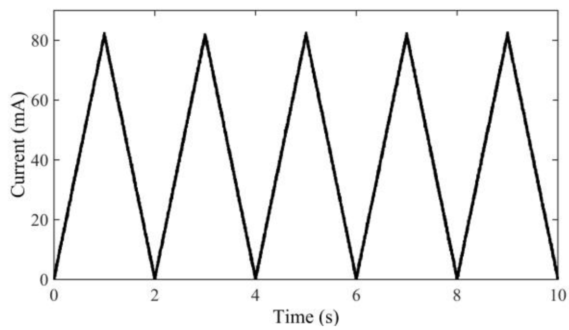

(a) Current applied to the force actuator

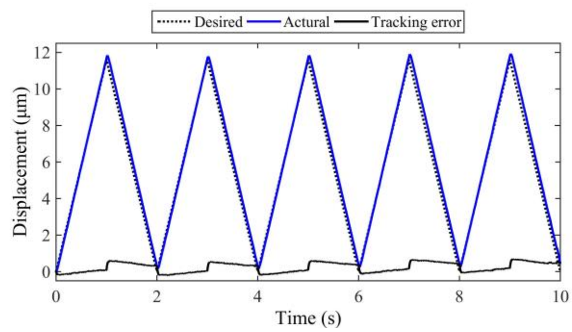

(b) Displacement of the central platform

Fig. 16 The response of the mechanism to 0.5 Hz triangular current

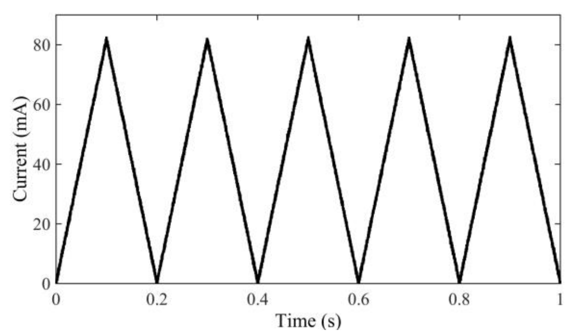

(a) Current applied to the force actuator

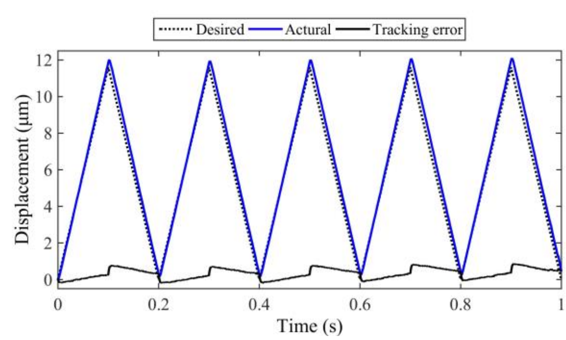

(b) Displacement of the central platform

Fig. 17 The response of the mechanism to 5 Hz triangular current

8. Conclusion

A novel 3-DOF suspension mechanism has been proposed, which is capable of providing 3-DOF movements. An electromagnetic force actuator is utilized to drive the 3-DOF suspension mechanism through a triangular flexure structure. FEA is conducted to investigate the characteristics of the electromagnetic force actuator. Utilizing stiffness matrix method, the analytical stiffness model of the 3-DOF suspension mechanism is established. Considering the mechanism as a 3-DOF lumped-mass-spring system, the dynamic model has been established. FEA is conducted to validate the established static and dynamic models. A prototype has been fabricated and experimentally tested. The agreements among the results demonstrate that the established models are appropriate. The experiment results show that the 3-DOF suspension mechanism provides a loading force in a range of up to 10 mN and has a working range in excess of 10 μm in Z axis. The first natural first natural frequency is measured to be 342 Hz in Z axis, attenuating the free oscillation of the mechanism and ensuring a fast response. Thus, the 3-DOF suspension mechanism has wide potentials for multi-function stylus profiling systems. Future work is directed towards hysteresis compensation of the 3-DOF suspension mechanism.

ACKNOWLEDGEMENT

This research is supported by National Natural Science Foundation of China (Nos. 51420105007, 51175372, 51275337, 51205279), National Key Special Project of Science and Technology of China (No. 2011ZX04016-011), Reserved Academic Program of Peiyang Scholar, and Program for New Century Excellent Talents in University (No. NCET-11-0374).

REFERENCES

1. Herzig, H. P., “Micro-optics: elements, systems and applications,” Taylor & Francis, London, 1997.
2. Fu, T. C., Suzuki, S., “Low stiction/low glide height head–disk interface for high-performance disk drives,” Journal of Applied physics, Vol. 85, No. 8, pp. 5600–5605, 1999.
3. Liu, X., Bell, T., Chetwynd, D. G., and Li, X. Y., “Characterisation of engineered surfaces by a novel four-in-one tribological probe microscope,” Wear, Vol. 255, No. 1-6, pp. 385–394, 2003.
4. Cui, Y. G., Arai, Y., Asai, T., Ju, B. G. and Gao, W., “A high-speed atomic force microscope for precision measurement of microstructured surfaces,” International Journal of Precision Engineering and Manufacturing, Vol. 9, No. 3, pp. 27-32, 2008.
5. Asai, T., Motoki, T., Gao, W., Ju, B. F. and Kiyono, S., “An AFM-based edge profile measuring instrument for diamond cutting tools,” International Journal of Precision Engineering, Vol. 8, No. 2, pp. 54-58, 2007.
6. Choi, J. H. and Korach, C. S., “Tip Bluntness Transition Measured with Atomic Force Microscopy and the Effect on Hardness Variation with Depth in Silicon Dioxide Nanoindentation,” International Journal of Precision Engineering and Manufacturing, Vol. 12, No. 2, pp. 345-354, 2011.

DOI: XXX-XXX-XXXX

7. Mate, C. M., McClelland, G. M., Erlanfsson, R. and Chiang, S., "Atomic-scale friction of a tungsten tip on a graphite surface," Physical Review Letters, Vol. 59, No. 17, pp. 1942–1945, 1987.

8. Heuberger, M., Dietler, G. and Schlabach, L., "Mapping the local Young's modulus by analysis of the elastic deformations occurring in atomic force microscopy," Nanotechnology, Vol. 6, No. 1, pp. 12–23, 1995.

9. Houston, J. E. and Michalske, T. A., "The interfacial-force microscope," Nature, Vol. 356, No. 6366, pp. 266-267,1992.

10. Lee, E. K., Kang, C. G. and Lee, S. M., "Evaluation of Mechanical Characteristics of the Plate-Type Polymer Hyperfine Pit Pattern by the Nanoindentation Process," International Journal of Precision Engineering and Manufacturing, Vol. 11, No. 3, pp. 461-468, 2010.

11. Liu, X. and Gao, F., "A novel multi-function tribological probe microscope for mapping surface properties," Measurement Science and technology, Vol. 15, No. 1, pp. 91–102, 2004.

12. Hong, K. S., Sohn, H. C. and Hedrick, J. K., "Modified skyhook control of semi-active suspensions: A new model, gain scheduling, and hardware-in-the-loop tuning," ASME Transactions, Journal of Dynamic Systems, Measurement, and Control, Vol. 124, No. 1, pp. 158-167, 2002.

13. Sohn, H. C., Hong, K. T., Hong, K. S. and Yoo, W. S. "An adaptive LQG control of semi- active suspension systems," International Journal of Vehicle Design, Vol. 34, No. 4, pp. 309-326, 2004.

14. Turnip, A., Park. S. and Hong, K. S., "Sensitivity control of a MR-damper semi-active suspension," International Journal of Precision Engineering and Manufacturing, Vol. 11, No. 2, pp. 209-218, 2010.

15. Nguyen, L. H. Hong, K. S. and Park, S., "Road-frequency adaptive control for semiactive suspension system," International Journal of Control, Automation, and Systems, Vol. 8, No. 5, pp. 1029-1038, 2010.

16. Turnip, A. and Hong, K. S., "Road-frequency based optimization of damping coefficients for semi-active suspension systems," International Journal of Vehicle Design, Vol. 63, No. 1, pp. 84-101, 2013.

17. Huan, Y., Zhang, T. and Yang, Y., "A moving-coil designed micro-mechanics tester with application on MEMS," Measurement Science and Technology, Vol. 18, No. 11, pp. 3612-3616, 2007.

18. www.hysitron.com

19. Kulkarni, A. V. and Bhushan, B., "Nano/picoindentation measurements on single-crystal aluminum using modified atomic force microscopy," Materials Letters, Vol. 29, No. 4-6, pp. 221-227, 1996.

20. Syed Asif, S. A., Wahl, K. J. and Colton, R. J., "Nanoindentation and contact stiffness measurement using force modulation with a capacitive load-displacement transducer," Review of Scientific Instruments, Vol. 70, No. 5, pp. 2408-2413, 1999.

21. Yu, N., Bonin, W. A. and Polycarpou, A. A., "High-resolution capacitive load-displacement transducer and its application in nanoindentation and adhesion force measurements," Review of Scientific Instruments, Vol. 76, No. 4, pp. 045109, 2005.

22. Gao, P. and Yuan, Z., "Development of a micromechanical probe-measuring instrument for surface properties characterization," Measurement Science and technology, Vol. 10, No. 8, pp. N105–N108, 1999.

23. Haitjema, H., Pril, W. O. and Schellekens, P. H. J., "A silicon-etched probe for 3-D coordinate measurements with an uncertainty below 0.1 μm," IEEE Transactions on Instrumentation and Measurement, Vol. 50, No. 6, pp. 1519-1523, 2001.

24. Haitjema, H., Pril, W. O. and Schellekens, P. H. J., "Development of a silicon-based nanoprobe system for 3-D measurements," CIRP Annals-Manufacturing Technology, Vol. 50, No. 1, pp. 365-368, 2001.

25. Balzer, F. G., Hausotte, T., Dorozhovets, N., Manske, E. and Jäger, G., "Tactile 3D microprobe system with exchangeable styli," Measurement Science and Technology, Vol. 22, No. 9, pp. 094018, 2011.

26. Sun, Y. F., Fowkes, C. R., Gindy, N. and Leach, R. K., "Variation risk analysis: MEMS fabrication tolerance for a micro CMM probe," The International Journal of Advanced Manufacturing Technology, Vol. 47, No. 9-12, pp. 1113-1120, 2010.

27. Smith, S. T., Chetwynd, D. G. and Bowen, D. K., "Design and assessment of monolithic high precision translation mechanisms," Journal of Physics E: Scientific Instruments, Vol. 20, No. 8, pp. 977-983, 1987.

28. Chetwynd, D. G., Liu, X. and Smith, S. T., "A controlled-force stylus displacement probe," Precision Engineering, Vol. 19, No. 2-3, pp. 105-111, 1996.

29. Smith, S. T. and Chetwynd, D. G., "Optimized magnet-coil force actuator and its application to precision elastic mechanisms," Proceedings of the Institution of Mechanical Engineers, Part C: Journal of Mechanical Engineering Science, Vol. 204, No. 4, pp. 243-253, 1990.

30. Pham, H. H. and Chen, I. M., "Stiffness modeling of flexure parallel mechanism," Precision Engineering, Vol. 29, No. 4, pp. 467–478, 2005.

31. Koseki, Y., Tanikawa, T., Koyachi, N. and Arai, T., "Kinematic Analysis of Translational 3-DOF Micro Parallel Mechanism Using Matrix Method," Advanced Robotics, Vol. 16, No. 3, pp. 251~264, 2002.

32. Hao, G. and Kong, X. "A novel large-range XY compliant parallel manipulator with enhanced out-of-plane stiffness," Journal of Mechanical Design, Vol. 134, No. 6, pp. 061009, 2012.